Published in final edited form as:
Arterioscler Thromb Vasc Biol. 2005 August ; 25(8): 1729–1735.

Mineral Volume and Morphology in Carotid Plaque Specimens Using High-Resolution MRI and CT

Ronald L. Wolf, **Suzanne L. Wehrli**, **Andra M. Popescu**, **John H. Woo**, **Hee Kwon Song**, **Alexander C. Wright**, **Emile R. Mohler III**, **John D. Harding**, **Eric L. Zager**, **Ronald M. Fairman**, **Michael A. Golden**, **Omaida C. Velazquez**, **Jeffrey P. Carpenter**, and **Felix W. Wehrli**
Departments of Radiology (R.L.W., A.M.P., J.H.W., H.K.S., A.C.W., F.W.W.), Cardiology (E.R.M., J.D.H.), Neurosurgery (E.L.Z.), and Vascular Surgery (R.M.F., M.A.G., O.C.V., J.P.C.), University of Pennsylvania Medical System, Philadelphia; and Children's Hospital of Philadelphia (S.L.W.), Penn.

Abstract

Objective—High-resolution MRI methods have been used to evaluate carotid artery atherosclerotic plaque content. The purpose of this study was to assess the performance of high-resolution MRI in evaluation of the quantity and pattern of mineral deposition in carotid endarterectomy (CEA) specimens, with quantitative micro-CT as the gold standard.

Methods and Results—High-resolution MRI and CT were compared in 20 CEA specimens. Linear regression comparing mineral volumes generated from CT (V_{CT}) and MRI (V_{MRI}) data demonstrated good correlation using simple thresholding (V_{MRI}=-0.01+0.98V_{CT}; R^2=0.90; threshold=4×noise) and k-means clustering methods (V_{MRI}=-0.005+1.38V_{CT}; R^2=0.93). Bone mineral density (BMD) and bone mineral content (BMC [mineral mass]) were calculated for CT data and BMC verified with ash weight. Patterns of mineralization like particles, granules, and sheets were more clearly depicted on CT.

Conclusions—Mineral volumes generated from MRI or CT data were highly correlated. CT provided a more detailed depiction of mineralization patterns and provided BMD and BMC in addition to mineral volume. The extent of mineralization as well as the morphology may ultimately be useful in assessing plaque stability.

Keywords

magnetic resonance imaging; computed tomography; carotid arteries; calcium

A significant fraction of all ischemic strokes is caused by carotid atherosclerosis. Degree of stenosis is a major risk factor, but factors unrelated to the extent of vascular constriction play a role in causing neurological symptoms, including the morphology and composition of the atherosclerotic plaque.[1,2] Components of plaque associated with symptoms ("vulnerable plaque") include surface ulceration, thinning of fibrous cap, presence of hemorrhage, lipid core, and inflammation and neovascularity.[3-6]

Dystrophic calcification (mineralization) and even lamellar bone have been described in carotid plaques.[7,8] There is evidence for an association between plaque lipid and dystrophic mineralization.[9] Using confocal microscopy, Sarig et al[10] found that cholesterol or associated lipids may act as a nucleus for hydroxyapatite crystal formation. It is unclear to what extent

Correspondence to Ronald L. Wolf, MD, PhD, University of Pennsylvania Medical Center, Section of Neuroradiology, Department of Radiology, 3400 Spruce St, Philadelphia, PA 19104. E-mail Ronald.Wolf@uphs.upenn.edu

carotid plaque calcification affects the risk of embolic stroke. Certain patterns of calcification may help grade lesions and provide an indicator of stability.[11]

The potential role of MRI for noninvasive assessment of plaque morphology and lesion burden quantification has been addressed in several investigations ex vivo and in vivo.[12-24] The appearance of plaque calcification has been described as uniformly dark in signal intensity on all MRI sequences.[18,25,26] However, there are other components of atherosclerotic plaque that may show decreased signal intensity on some or all pulse sequences; for example, solid cholesterol hydrate may be present and plaque lipids may exhibit T2 shortening secondary to liquid crystal behavior, depending on the lipid composition and cholesterol content.[20,27] Induced magnetic field inhomogeneities caused by differences in diamagnetic susceptibility between soft tissue and mineral may, in principle, lead to overestimation of mineral content on MRI. Alternatively, some forms of calcification or ossification could conceivably not appear dark on MRI. The purpose of this study was to assess the performance of high-resolution MRI in evaluation of the quantity and pattern of mineral deposition in carotid endarterectomy (CEA) specimens, with quantitative micro-CT as the gold standard.

Methods

Subjects

Specimens were obtained from 18 subjects undergoing CEA (12 males and 6 females; mean age of 68 years, range 55 to 83). For 2 subjects, the specimen was retrieved in 2 parts and scanned separately, treated as separate specimens for imaging purposes (20 specimens imaged). All studies were performed within institutional review board guidelines, and consent was obtained. Clinical information is summarized in Table 1.

Magnetic Resonance Imaging

Specimen MRI was performed on a DMX-400 9.4-T vertical-bore NMR spectrometer/microimaging system (Bruker, Inc.), imaging in saline at 37°C in the 15-mm radiofrequency coil insert. Specimen imaging consisted of short-repetition time (TR) spin echo (TR=700 ms; echo time [TE]=12 to 13 ms) and long-TR multiecho spin echo (5 evenly spaced echoes; TR=2000 ms; TE=9 to 10 ms for first echo), 4 averages for long and short TR sequences. Diffusion-weighted images (DWI) were also acquired (TR=2000 ms; TE=36 ms, b=1044 s/mm^2, 4 averages). Section thickness was 0.5 mm, field of view (FOV) 15 mm, and matrix 256×256 for an in-plane resolution of 59 μm (voxel volume 1.72×10^{-3} mm^3). Contiguous 0.5-mm sections were obtained in 2 interleaved acquisitions.

CT Imaging

Specimen CT studies were performed on an MS8 micro-CT specimen scanner (GE Medical Systems, formerly Enhanced Vision Systems).[28] Data were acquired using the following parameters: volumetric cone-beam acquisition, 80 kVp and 80 μA, FOV 15 or 33 mm (depending on size of specimen), 360° acquisition, 720 views, 0.5° angle increment, 3 averages, and 0.020-inch thick aluminum filter. Volumes were reconstructed using a Feldkamp cone beam algorithm, with typical resolution of 33-μm isotropic voxels (voxel volume 3.59×10^{-5} mm^3). A hydroxyapatite phantom with a known bone mineral density (BMD) of 1073 mg/mL was scanned with the same parameters for calibration of reconstruction to obtain quantitative analysis of mineral content. Another phantom with serial dilutions of K_2HPO_4 solution ranging from 0 to 1000 mg/mL was also scanned to ensure linearity of the absorbance over a range of mineral densities because of possible beam-hardening effects.[29] K_2HPO_4 is known to have the same attenuation per unit mass as bone mineral. The specimen and phantoms were scanned in air within a sealed tube to allow visualization of specimen soft tissues as well as calcifications.

MRI Analysis

Mineral volume was calculated using 2 different approaches, one based on a simple thresholding algorithm and the other based on a k-means clustering algorithm. For the thresholding approach, the first echo of the multiecho sequence (first of 5 images or echoes=proton density-weighted [PDW] image) was used. Data were processed using custom software developed using IDL (Research Systems, Inc.). For each specimen study, the background noise value was estimated by the mean signal intensity of the PDW image in a 20×20-pixel region of interest (ROI) near the corner of the middle rectangular slice, outside of the object (the cylindrical container with saline and specimen). A binary mask was first generated for each section to remove background pixels. Mineral maps were generated by a 2-step process: (1) a preliminary mineral map was created by finding all pixels within the specimen, the values of which were less than a user-specified threshold (a fixed multiple of the background noise estimate); and (2) this raw map was then digitally processed by a clustering algorithm that applied a morphological opening operator with 2-pixel structuring elements (equivalent to an erosion followed by a dilation) so that isolated pixels would be discarded from the final mineral map.

Thresholds of 4 and 8× the background noise were chosen based on previous work and on initial visual comparison of the mask with expected mineralized regions (ie, those with markedly decreased signal intensity; Figure 1).[18] Gas bubble formation was unavoidable in magnetic resonance (MR) acquisitions, and these were sometimes mistaken for mineralized pixels by this algorithm. The appearance of bubbles was usually distinct, either located outside of the specimen or with an associated flare artifact at the bubble edge (Figure 1). The user could manually eliminate these pixels from further analysis. For each threshold, pixels identified as mineral were recorded for each imaging section and summed, and mineral volume calculated by multiplying the number of mineralized pixels by voxel volume.

For the k-means clustering approach,[30] data were processed using ImageJ with a k-means clustering plug-in (public domain image processing and analysis software developed in Java; National Institutes of Health). A multicontrast image stack was created for each specimen using 5 different image contrast weightings: the first, third, and fifth echo of the multiecho sequence (PDW, intermediate-weighted, and T2-weighted [T2W]); T1-weighted (T1W); and DWI. The k-means algorithm allows segmentation of multicontrast images, in which each voxel is represented by a vector of n contrasts (n=5 in this implementation as detailed above). Voxels are assigned to a cluster based on proximity to the cluster centroids. The centroids are initiated with a random seed (the same in each case for this study) and then iteratively optimized until tolerance criteria are met (cluster center tolerance 0.0001 for this study). Four clusters were allowed. A reproducible assignment of mineralized voxels to 1 cluster was obtained in this manner (the other 3 cluster assignments were not evaluated in this study; Figure 1).

CT Image Analysis

Microview (GE Medical Systems, freely distributed 3D volume viewer) was used to generate mineral mass, volume, and BMD. Briefly, a cylindrical 3D ROI was first positioned to include the CEA specimen. In some cases, the specimen could not be completely included in the MRI FOV. In these cases, the analyzed CT volume was matched to the imaged MRI volume. Mineral mass in each voxel was calculated based on a 2-component model: a cortical bone equivalent (hydroxyapatite density 1073 mg/mL) and a soft tissue or water component (hydroxyapatite density 0 mg/mL). Mean attenuation in each voxel in the 3D ROI was converted to density by interpolating along this line. Density multiplied by voxel volume yielded voxel mass. A standard attenuation value midway between air and soft tissue attenuation of -500 apparent density units (ADU) was chosen to exclude air-containing voxels from the calculation. The sum of voxel masses yields total mineral mass or bone mineral content (BMC).

The volume fraction of mineral in the original 3D ROI can be calculated by identifying a threshold between soft tissue and mineral. A threshold of 2500 ADU was chosen empirically to insure inclusion of mineral containing voxels, corresponding to a point between peaks in the histogram for mineral-containing structures and for soft tissue. Mineral volume is the product of the original 3D ROI volume and the volume fraction of mineral in the ROI. The BMD corresponding to only the mineralized portion of the specimen was calculated for each specimen by dividing mineral mass (BMC) by mineral volume.

Ash Weights and Chemical Analysis

BMC was checked against ash weights for the first 12 subjects. After imaging, specimens were frozen in liquid nitrogen and pulverized with a mortar and pestle. Lipids were extracted using a modified Folch technique[31] for use in a separate study. Tissue fragments were retained, and solvents were evaporated. The fragments were dried, weighed at room temperature, and transferred to crucibles. They were placed in a furnace for 24 hours at 540°C. The specimen fragments and crucibles were weighed after they had cooled to room temperature and ash weight calculated by subtracting crucible tare weight. Specimen fragments and crucibles were stored and transferred in the presence of a dessicant at all times. The ashed specimens were then analyzed for calcium and phosphorus content using inductively coupled plasma-mass spectrometry (ICP-MS). For ICP-MS measurements, digestion of ashed specimens was first performed in a closed vessel nitric acid procedure. Dectection and quantitation of calcium and total phosphorus were based on the ^{44}Ca and ^{31}P ions using scandium as the internal standard. Results were generated in parts per million and the mass of each element then calculated based on the mass of the ashed specimen.

Data Analysis

A statistical analysis software package (JMP Start Statistics, second edition; SAS Institute) was used to calculate a straight-line least squares regression comparing mineral volumes generated from MRI versus CT data. The same approach was used to compare measured BMD with control phantom BMD samples and to compare calculated BMC with ash weight and mineral content measured with ICP-MS.

Results

On visual inspection of micro-MR images compared with micro-CT images, mineral appeared as regions of markedly decreased signal intensity on micro-MR images and matched regions of increased attenuation on CT. Finer detail regarding pattern of mineralization was evident on micro-CT images, in which particles, granules, and sheets were clearly visualized (Figure 2).

Different patterns of mineralization could be segmented on the basis of the histogram. In Figure 3, color overlays corresponding to lower (≈2500 to 3800 ADU), middle (≈3800 to 5500 ADU), and upper (>5500) sections of mineral-containing bins from the sample histogram are displayed with the native image for 3 locations. Less dense, more amorphous and particulate patterns fell into the first (lower) range, whereas denser-appearing mineralization corresponded to middle and upper ranges. BMD from a small ROI in the more amorphous or particulate region was 771 mg/mL. Regions with denser, sheet-like appearance showed BMD at 1019 mg/mL. In a more sclerotic focus, BMD was 1462 mg/mL. Table 2 lists mineral volumes derived from MRI and CT data, as well as mass and BMD measurements from CT data for the specimens.

Figure 4 shows plots of mineral volumes and corresponding linear regressions for MRI versus CT (V_{MRI} and V_{CT}, respectively) using a threshold for MRI of 4×background noise and using the k-means clustering algorithm. MRI agreed well with CT measurements at this threshold

(linear fit V_{MRI}=-0.01+0.98V_{CT}; R^2=0.90; F=166.62; P<0.0001). Mineral volume was overestimated by MRI compared with CT for the threshold of 8×background noise (linear fit V_{MRI}=-0.01+1.49V_{CT}; R^2=0.86; F=110.51; P<0.0001) and for the k-means clustering approach (linear fit V_{MRI}=-0.005+1.38V_{CT}; R^2=0.93; F=243.0; P<0.0001).

BMC showed good agreement compared with specimen ash weight for the 12 specimens for which ash weights were obtained (linear fit BMC=16.04+0.97ash weight; R^2=0.98; F=540.72; P<0.0001; Table 2). Calculated BMD of the calibration phantom and the K_2HPO_4 dilutions compared with known concentrations demonstrated an excellent linear relationship (calculated BMD=30.78+0.963control BMD; R^2=0.99; F=912.29; P<0.0001).

Calcium and phosphorus content of the ashed specimen are also listed in Table 2. One sample (subject 5) was too small for accurate quantitation of phosphorus. The mean ratio of the masses of calcium to phosphorus (Ca/P) in the other 11 ashed specimens was 2.14, which agrees with the expected Ca/P ratio of 2.15 in hydroxyapatite. Comparing calculated BMC with expected mineral mass generated by dividing the calcium mass by 0.40 (calcium fraction in hydroxyapatite) also demonstrated an excellent linear relationship (calculated BMC=19.73 +1.12expected BMC; R^2=0.97; F=387.12; P<0.0001), although CT overestimated mineral content compared with chemical analysis.

Discussion

It is believed that atherosclerotic calcification is more regulated and organized than originally thought, as opposed to a passive process.[32] Progression in extent and changes in morphology of calcifications in plaque have been described as atherosclerotic plaques become more advanced and as patients age. Initially, stippled calcifications can be seen as early as in type III lesions, progressing to more solid calcifications and bone in types IV through VII.[11,33] It is currently unclear to what extent the morphology and the presence or quantity of calcification in carotid plaque affect the risk of embolic stroke.

In this study, mineral in CEA plaque specimens was demonstrated with MRI, and measures of mineral volume generated with 2 segmentation approaches were highly correlated with CT measures of mineral volume. The relationship was closest to identity for a simple thresholding method of 4×background noise, whereas inspection of the segmented images and micro-CT images in this case suggested that much of the apparently mineralized material was excluded (Figures 1 and 4). Using a threshold of 8×background noise or a k-means clustering algorithm, the segmented MR images appeared to match micro-CT images more closely on visual inspection, but the slope of the regression line was >1 (1.49 and 1.38 for 8×background noise thresholding and k-means clustering approaches, respectively; Figures 1 and 4).

One might expect an exaggeration of extent of mineralization because of heterogeneous magnetic susceptibility around particulate calcifications and the decreased signal intensity associated with other short T2 species in the specimen like cholesterol crystals or solid/semisolid phase lipids.[20,27,34] At least for the thresholding method, the comparison was with only the first echo (TE=9 to 10 ms) of a multiecho spin echo technique, which would minimize signal loss from susceptibility-induced gradients. However, longer TE sequences incorporated into the k-means clustering approach may have had an effect in this regard. Partial volume effects likely played a role in either case. The resolution of the MRI data (voxel volume 1.72×10^{-3} mm^3) was lower than that of the CT data (voxel volume 3.59×10^{-5} mm^3), so that a voxel with only a small fractional mineral occupancy labeled as mineral would exaggerate actual mineral volume for MRI measurements relative to CT measurements. We used multiplanar (2D) MR acquisitions, but other sequences such as 3D gradient echo acquisitions may be more accurate in this light.[26] Shinnar et al used a threshold of 4×background noise on

a PDW image for calcification thresholds,[18] which showed good agreement for our data compared with CT (Figure 4) but appeared to underestimate apparent mineralization on visual inspection (Figure 1). Timing parameters for the PDW spin echo images were similar, and field strength was identical, although Shinnar used a single echo spin echo sequence.

Although not apparent in this small data set, mineral may not necessarily appear dark on all imaging sequences. Henkelman et al[35] examined the concentration-dependent signal intensity of hydroxyapatite at 1.5 T and found that T1 decreased as concentration of hydroxyapatite increased, leading to increased signal intensity on T1W images. T1 shortening was dependent not only on concentration of hydroxyapatite but also on surface area of mineral. This only occurs to a point because signal loss attributable to decreased proton density and decreased T2 will eventually dominate effects on signal intensity. The signal intensity of mineral on T2W images can also be variable and, in some cases, is increased although usually decreased.[35,36] Marrow inclusions may be present in atherosclerotic ossification,[37,38] although it is uncertain to what extent the presence of these inclusions could alter signal intensity. In summary, depending on the concentration, morphology, and environment of mineral in atherosclerotic plaques, the signal intensity of the mineral could vary.

One could consider that CT measurements underestimated mineral volume instead of overestimation with MRI, although this is less likely. Calculations of mineral concentration were checked against known concentrations of a hydroxyapatite mimic at 1073 mg/mL and also K_2HPO_4 dilutions.[29] Also, ash weights showed good agreement with mineral mass calculated on the basis of these assumptions. Calibration and verification of CT results was based on the assumption that the mineral in the specimen is primarily hydroxyapatite.[39] This was validated by ICP-MS measurements of calcium and phosphorus content, in which Ca/P ratios were consistent with a primarily hydroxapatite mineral content. The ICP-MS estimates of mineral mass are lower than those obtained by quantitative micro-CT and ash weight, although there is a very high correlation among all 3 types of measurements. The lower values obtained by mass spectrometry can be explained by the well-known fact that bone and dystrophic calcification (deposited by osteoblasts) consist of a nonstoichiometric calcium apatite in which some anionic and cationic lattice positions can be occupied by other ions. Because in our assay only phosphorus and calcium were measured with ICP-MS, this method could underestimate the actual mineral content. The presence of noncombustible material in the specimen preparation, such as buffer salts, could also have contributed to the discrepancy compared with ash weight.

Depiction of mineralization patterns was quite detailed on micro-CT images, in which particles, granules, and larger sheets were seen. Presence of large calcific deposits like the larger granules and sheets correlates with older age and histological types V, VI, or VII.[7,8,32,33] Certain patterns of mineralization may help grade lesions and perhaps provide an indicator of stability.[11] For example, Hunt et al found bone more often in stable plaques compared with unstable plaques, and patients with large granular calcifications in plaques had fewer ischemic events. Huang et al reported that increases in percent area of plaque occupied by calcium in coronary plaques was associated with decreased stress in the plaque, whereas increased plaque lipid content was correlated with increased stress.[40] On the other hand, some investigators argue that certain types of calcifications may increase risk.[32,33] For example, a shearing plane can be created between calcified and noncalcified plaque, predisposing to rupture in response to a stress such as angioplasty.[41] Even if increased calcium in plaques in one form or another can be shown to stabilize plaque, the fact remains that increased calcium content can still be a marker for more severe local or systemic atherosclerotic disease.[40]

Electron beam CT-derived coronary artery calcium scores have been shown to correlate with extent of coronary atherosclerosis, and this technique has been used to indirectly assess the

quantity of coronary plaque and to predict risk of future events.[42] Peripheral arteries (including carotid arteries) and the aorta can also be assessed in this way, and peripheral arterial calcification correlates with coronary artery calcium.[43] Multidetector CT was used recently to calculate calcium content in CEA specimens.[44] They found that volume scores were not as reliable as mineral mass. Mineral mass can be calculated from our CT data, but volume quantitation seemed to be the best way to initially compare MR and CT. CT angiography has become increasingly used in the last decade. Similar to the MR techniques listed above, CT angiography provides a 3D data set, which contains detailed information about not only the lumen but also about the vessel wall. Because the role of calcification (mineralization) may prove important for determining plaque stability, CT techniques would seem well suited for this application. Plaque density (aside from mineralization) may also be useful.[45]

A limitation of this study includes difficulties with registration between MRI and CT. Because of scanner configurations, the specimen had to be loaded into different holding devices. Therefore, positioning was difficult to match exactly, and deformation of the surgical specimens was often different. However, comparisons between calculated mineral volume, BMD, and BMC in specimens with MR versus CT should still be valid because the same overall volume was compared, and these values do not require a slice-by-slice registration. Another problem was bubble formation during MRI studies at 37°C. Although labor-intensive, this could be accounted for during the image analysis step. Although care was taken to eliminate bubbles before image acquisition, this problem could have been further minimized by degassing the sample and buffer under low vacuum. An alternative solution is currently in use, in which studies are now performed in Fomblin (perfluoro polyether) instead of saline to avoid this problem and to improve contrast between specimen and background. Finally, the resolution obtainable in this study with ex vivo MRI and CT is not currently possible in vivo, and thus, not yet directly applicable in a clinical setting. Comparison of preoperative in vivo imaging with ex vivo specimen imaging is currently under way.

In conclusion, mineral volumes generated from MRI or CT data are highly correlated, but MR estimates of mineral volume appear to be sensitive to the method chosen for segmentation. CT provides a detailed depiction of mineralization patterns and allows for generation of mineral density and mineral mass measures in addition to mineral volume. The extent of mineralization as well as the morphology may be useful in assessing plaque stability.

Acknowledgments

This study was supported in part by National Institutes of Health grants K23 NS43381 and R01 HL68908, K25 EB001427, and KO8 HL03974, and the Mary L. Smith Charitable Lead Trust. The authors thank Hualei Zhang for assistance with micro-CT calibrations.

References

1. Fayad ZA, Fuster V. Clinical imaging of the high-risk or vulnerable atherosclerotic plaque. Circ Res 2001;89:305–316. [PubMed: 11509446]
2. Stary HC. Natural history and histological classification of atherosclerotic lesions: an update. Arterioscler Thromb Vasc Biol 2000;20:1177–1178. [PubMed: 10807728]
3. Davies MJ, Richardson PD, Woolf N, Katz DR, Mann J. Risk of thrombosis in human atherosclerotic plaques: role of extracellular lipid, macrophage, and smooth muscle cell content. Br Heart J 1993;69:377–381. [PubMed: 8518056]
4. Fuster V, Badimon L, Badimon JJ, Chesebro JH. The pathogenesis of coronary artery disease and the acute coronary syndromes (1). N Engl J Med 1992;326:242–250. [PubMed: 1727977]
5. Fuster V, Badimon L, Badimon JJ, Chesebro JH. The pathogenesis of coronary artery disease and the acute coronary syndromes (2). N Engl J Med 1992;326:310–318. [PubMed: 1728735]
6. Kullo IJ, Edwards WD, Schwartz RS. Vulnerable plaque: pathobiology and clinical implications. Ann Intern Med 1998;129:1050–1060. [PubMed: 9867761]

7. Jeziorska M, McCollum C, Wooley DE. Observations on bone formation and remodeling in advanced atherosclerotic lesions of human carotid arteries. Virchows Arch 1998;433:559–565. [PubMed: 9870690]
8. Jeziorska M, McCollum C, Woolley DE. Calcification in atherosclerotic plaque of human carotid arteries: associations with mast cells and macrophages. J Pathol 1998;185:10–17. [PubMed: 9713354]
9. Watson KE, Demer LL. The atherosclerosis-calcification link? Curr Opin Lipidol 1996;7:101–104. [PubMed: 8743903]
10. Sarig S, Weiss TA, Katz I, Kahana F, Azoury R, Okon E, Kruth HS. Detection of cholesterol associated with calcium mineral using confocal fluorescence microscopy. Lab Invest 1994;71:782–787. [PubMed: 7967529]
11. Hunt JL, Fairman R, Mitchell ME, Carpenter JP, Golden M, Khalapyan T, Wolfe M, Neschis D, Milner R, Scoll B, Cusack A, Mohler ER III. Bone formation in carotid plaques: a clinicopathologic study. Stroke 2002;33:1214–1219. [PubMed: 11988593]
12. Corti R, Fuster V, Fayad ZA, Worthley SG, Helft G, Smith D, Weinberger J, Wentzel J, Mizsei G, Mercuri M, Badimon JJ. Lipid lowering by simvastatin induces regression of human atherosclerotic lesions: two years' follow-up by high-resolution noninvasive magnetic resonance imaging. Circulation 2002;106:2884–2887. [PubMed: 12460866]
13. Fayad ZA, Fallon JT, Shinnar M, Wehrli S, Dansky HM, Poon M, Badimon JJ, Charlton SA, Fisher EA, Breslow JL, Fuster V. Noninvasive In vivo high-resolution magnetic resonance imaging of atherosclerotic lesions in genetically engineered mice. Circulation 1998;98:1541–1547. [PubMed: 9769308]
14. Fuster V, Corti R, Fayad ZA, Schwitter J, Badimon JJ. Integration of vascular biology and magnetic resonance imaging in the understanding of atherothrombosis and acute coronary syndromes. J Thromb Haemost 2003;1:1410–1421. [PubMed: 12871275]
15. Gold GE, Pauly JM, Glover GH, Moretto JC, Macovski A, Herfkens RJ. Characterization of atherosclerosis with a 1.5-T imaging system. J Magn Reson Imaging 1993;3:399–407. [PubMed: 8448403]
16. Martin AJ, Gotlieb AI, Henkelman RM. High-resolution MR imaging of human arteries. J Magn Reson Imaging 1995;5:93–100. [PubMed: 7696815]
17. Mohiaddin RH, Firmin DN, Underwood SR, Abdulla AK, Klipstein RH, Rees RS, Longmore DB. Chemical shift magnetic resonance imaging of human atheroma. Br Heart J 1989;62:81–89. [PubMed: 2765330]
18. Shinnar M, Fallon JT, Wehrli S, Levin M, Dalmacy D, Fayad ZA, Badimon JJ, Harrington M, Harrington E, Fuster V. The diagnostic accuracy of ex vivo MRI for human atherosclerotic plaque characterization. Arterioscler Thromb Vasc Biol 1999;19:2756–2761. [PubMed: 10559022]
19. Toussaint JF, LaMuraglia GM, Southern JF, Fuster V, Kantor HL. Magnetic resonance images lipid, fibrous, calcified, hemorrhagic, and thrombotic components of human atherosclerosis in vivo. Circulation 1996;94:932–938. [PubMed: 8790028]
20. Toussaint JF, Southern JF, Fuster V, Kantor HL. T2-weighted contrast for NMR characterization of human atherosclerosis. Arterioscler Thromb Vasc Biol 1995;15:1533–1542. [PubMed: 7583524]
21. Yuan C, Beach KW, Smith LH Jr, Hatsukami TS. Measurement of atherosclerotic carotid plaque size in vivo using high resolution magnetic resonance imaging. Circulation 1998;98:2666–2671. [PubMed: 9851951]
22. Yuan C, Murakami JW, Hayes CE, Tsuruda JS, Hatsukami TS, Wildy KS, Ferguson MS, Strandness DE Jr. Phased-array magnetic resonance imaging of the carotid artery bifurcation: preliminary results in healthy volunteers and a patient with atherosclerotic disease. J Magn Reson Imaging 1995;5:561–565. [PubMed: 8574042]
23. Yuan C, Tsuruda JS, Beach KN, Hayes CE, Ferguson MS, Alpers CE, Foo TK, Strandness DE. Techniques for high-resolution MR imaging of atherosclerotic plaque. J Magn Reson Imaging 1994;4:43–49. [PubMed: 8148555]
24. Zhao XQ, Yuan C, Hatsukami TS, Frechette EH, Kang XJ, Maravilla KR, Brown BG. Effects of prolonged intensive lipid-lowering therapy on the characteristics of carotid atherosclerotic plaques in vivo by MRI: a case-control study. Arterioscler Thromb Vasc Biol 2001;21:1563–1564. [PubMed: 11597925]

25. Clarke SE, Hammond RR, Mitchell JR, Rutt BK. Quantitative assessment of carotid plaque composition using multicontrast MRI and registered histology. Magn Reson Med 2003;50:1199–1208. [PubMed: 14648567]
26. Coombs BD, Rapp JH, Ursell PC, Reilly LM, Saloner D. Structure of plaque at carotid bifurcation: high-resolution MRI with histological correlation. Stroke 2001;32:2516–2521. [PubMed: 11692010]
27. Pearlman JD, Zajicek J, Merickel MB, Carman CS, Ayers CR, Brookeman JR, Brown MF. High-resolution 1H NMR spectral signature from human atheroma. Magn Reson Med 1988;7:262–279. [PubMed: 3205143]
28. Marxen M, Thornton MM, Chiarot CB, Klement G, Koprivnikar J, Sled JG, Henkelman RM. Micro-CT scanner performance and considerations for vascular specimen imaging. Med Phys 2004;31:305–313. [PubMed: 15000616]
29. Nuzzo S, Peyrin F, Cloetens P, Baruchel J, Boivin G. Quantification of the degree of mineralization of bone in three dimensions using synchrotron radiation microtomography. Med Phys 2002;29:2672–2681. [PubMed: 12462734]
30. Jain, AK.; Dubes, RC. Algorithms for Clustering Data. Prentice-Hall, Inc.; Englewood Cliffs, NJ: 1988.
31. Folch J, Mees M, Sloane Stanley GH. A simple method for the isolation and purification of total lipides from animal tissues. J Biol Chem 1957;226:497–509. [PubMed: 13428781]
32. Wexler L, Brundage B, Crouse J, Detrano R, Fuster V, Maddahi J, Rumberger J, Stanford W, White R, Taubert K. Coronary artery calcification: pathophysiology, epidemiology, imaging methods, and clinical implications. Circulation 1996;94:1175–1192. [PubMed: 8790070]
33. Stary HC The development of calcium deposits in atherosclerotic lesions and their persistence after lipid regression. Am J Cardiol 2001;88(suppl):16E–19E.
34. Hopkins JA, Wehrli FW. Magnetic susceptibility measurement of insoluble solids by NMR: magnetic susceptibility of bone. Magn Reson Med 1997;37:494–500. [PubMed: 9094070]
35. Henkelman RM, Watts JF, Kucharczyk W. High signal intensity in MR images of calcified brain tissue. Radiology 1991;179:199–206. [PubMed: 1848714]
36. Avrahami E, Cohn DF, Feibel M, Tadmor R. MRI demonstration and CT correlation of the brain in patients with idiopathic intracerebral calcification. J Neurol 1994;241:381–384. [PubMed: 7931433]
37. Sands SF, Farmer P, Alvarez O, Keller IA, Gorey MT, Hyman RA. Fat within the falx: MR demonstration of falcine bony metaplasia with marrow formation. J Comput Assist Tomogr 1987;11:602–605. [PubMed: 3110222]
38. Deneke T, Langner K, Grewe PH, Harrer E, Muller KM. Ossification in atherosclerotic carotid arteries. Z Kardiol 2001;90:106–115. [PubMed: 11374022]
39. Schmid K, McSharry WO, Pameijer CH, Binette JP. Chemical and physicochemical studies on the mineral deposits of the human atherosclerotic aorta. Atherosclerosis 1980;37:199–210. [PubMed: 7426095]
40. Huang H, Virmani R, Younis H, Burke AP, Kamm RD, Lee RT. The impact of calcification on the biomechanical stability of atherosclerotic plaques. Circulation 2001;103:1051–1056. [PubMed: 11222465]
41. Honye J, Mahon DJ, Jain A, White CJ, Ramee SR, Wallis JB, al-Zarka A, Tobis JM. Morphological effects of coronary balloon angioplasty in vivo assessed by intravascular ultrasound imaging. Circulation 1992;85:1012–1025. [PubMed: 1537099]
42. Arad Y, Spadaro LA, Roth M, Scordo J, Goodman K, Sherman S, Lledo A, Lerner G, Guerci AD. Correlations between vascular calcification and atherosclerosis: a comparative electron beam CT study of the coronary and carotid arteries. J Comput Assist Tomogr 1998;22:207–211. [PubMed: 9530380]
43. Simon A, Giral P, Levenson J. Extracoronary atherosclerotic plaque at multiple sites and total coronary calcification deposit in asymptomatic men. Association with coronary risk profile. Circulation 1995;92:1414–1421. [PubMed: 7664421]
44. Hoffman U, Kwait DC, Handwerker J, Chan R, Lamuraglia G, Brady TJ. Vascular calcification in ex vivo carotid specimens: precision and accuracy of measurements with multi-detector row CT. Radiology 2003;229:375–381. [PubMed: 14526093]

45. Oliver TB, Lammie GA, Wright AR, Wardlaw J, Patel SG, Peek R, Ruckley CV, Collie DA. Atherosclerotic plaque at the carotid bifurcation: CT angiographic appearance with histopathologic correlation. AJNR Am J Neuroradiol 1999;20:897–901. [PubMed: 10369363]

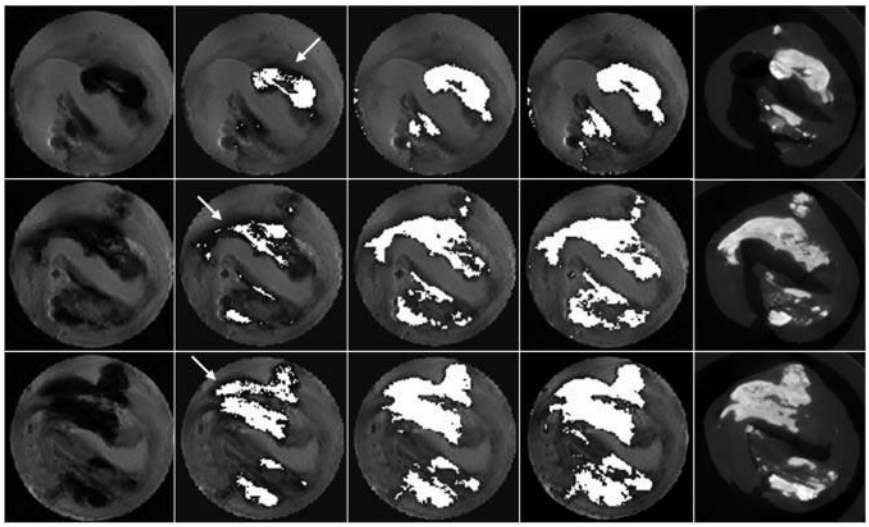

Figure 1.
MRI mineral volume calculation. PDW image, 4 and 8× background noise threshold segmented images, k-means clustering segmented image, and micro-CT images are shown (left to right) for 3 locations (top to bottom). In some regions, visually apparent mineralization was not segmented, especially for the lower threshold (white arrows).

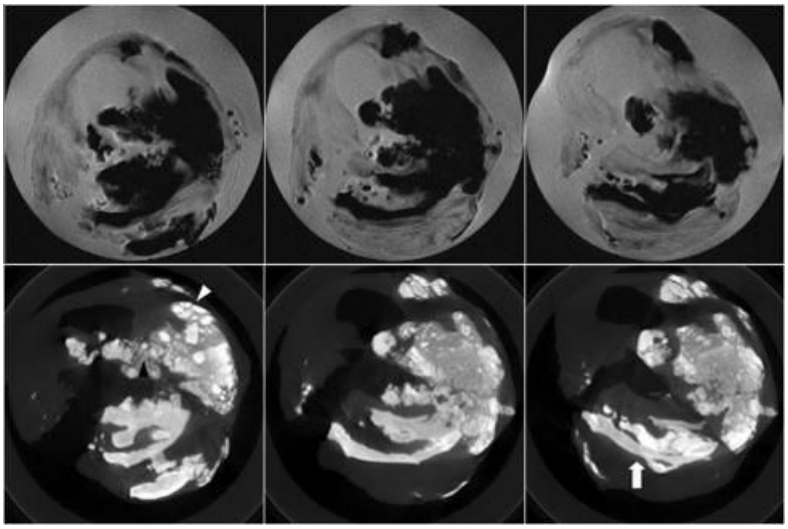

Figure 2.
Micro-MR and micro-CT images. Consecutive axial PDW images (top) show dark signal intensity in regions clearly calcified in micro-CT images (bottom). Fine detail regarding patterns of mineralization with particles (black arrowhead), granules (white arrowhead), and sheets (white arrow) is evident on micro-CT images.

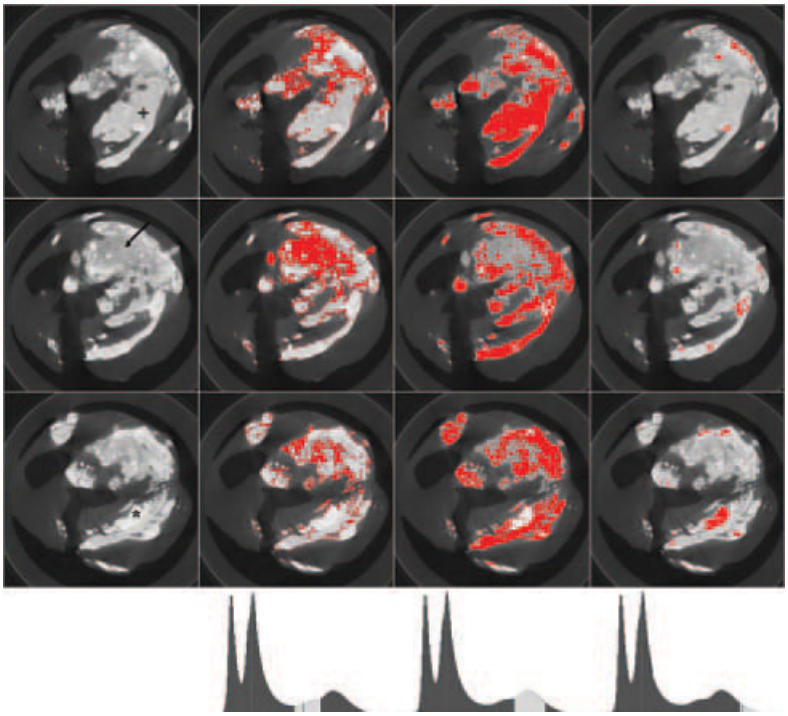

Figure 3.

Mineralization patterns. From left to right, native image, lower (≈2500 to 3800 ADU), middle (≈3800 to 5500 ADU) and upper (>5500) ranges of mineral-containing bins of histogram (bottom row) are shown for 3 imaging locations (top to bottom). BMD varied for particulate (arrow; 771 mg/mL), sheet-like (+; 1019 mg/mL), and sclerotic regions (*; 1462 mg/mL).

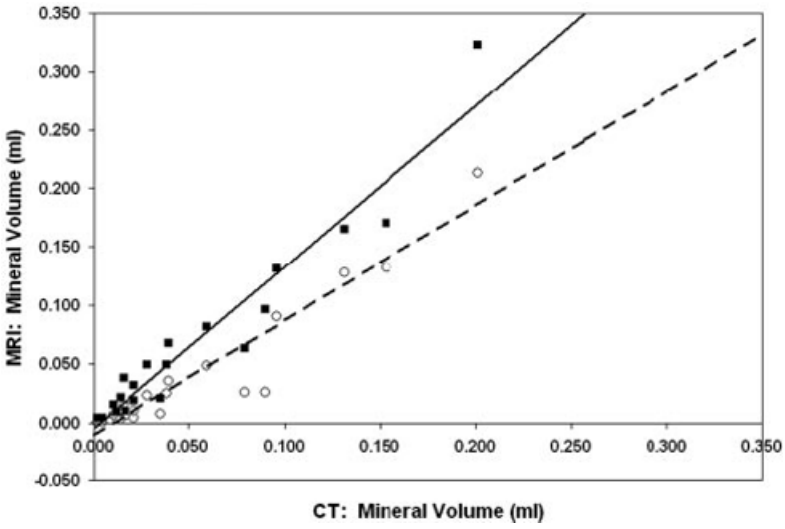

Figure 4.

MRI threshold method at 4×background noise vs CT (○), with linear fit (dashed line): V_{MRI}=-0.01+0.98V_{CT}; R^2=0.90; F=166.62; P<0.0001. MRI k-means clustering method versus CT (■), with linear fit (solid line): V_{MRI}=-0.005+1.38V_{CT}; R^2=0.93; F=243.00; P<0.0001.

TABLE 1

Clinical Data

Subject	Sex	Age	PAD	CAD	DM	Tobacco	FH	HTN	Stroke	TIA	Statin
1	F	74	-	-	-	N	-	+	-	-	-
2	M	74	+	+	+	C	-	+	-	-	+
3	F	81	-	+	+	F	+	+	-	-	+
4	F	63	-	-	+	F	-	+	-	-	+
5	M	60	-	-	-	F	-	+	-	-	+
6	M	72	+	+	+	F	-	-	-	-	+
7	F	60	-	-	+	F	-	-	-	-	-
8	F	68	-	-	-	F	-	+	-	-	+
9	M	64	-	+	-	F	-	+	-	-	-
10	M	64	-	+	-	F	+	+	-	-	+
11	M	73	-	+	-	F	-	+	-	+	+
12	M	63	-	-	-	F	-	-	-	-	-
13	M	67	+	+	-	C	-	+	-	-	+
14	M	62	-	-	-	F	-	+	-	-	+
15	F	59	-	-	+/-	F	+	+	-	+	+
16	M	83	-	-	-	F	+	+	-	-	+
17	M	55	+	+	+	F	+	+	-	-	+
18	M	81	-	-	+	F	+	+	+	+	+

PAD indicates peripheral artery disease; CAD, coronary artery disease; DM, diabetes mellitus; FH, family history CAD; HTN, hypertension; TIA, transient ischemic attack; Statin, currently medicated with statin drug; M, male; F, female.

Regarding tobacco use, N indicates never; C, current; F, former.

TABLE 2

Specimen Analysis

Subject	MRI Volume (mL)			CT			Ash Weight (mg)	Chemical Analysis (mg)	
	4×	8×	k-means	Volume (mL)*	BMD (mg/mL)	BMC (mg)		Ca	P
1	0.015	0.038	0.038	0.015	3434.286	53.225	20.10	6.16	2.95
2	0.036	0.098	0.068	0.039	1888.235	74.461	55.00	17.06	8.06
3	0.007	0.012	0.020	0.036	1497.009	53.185	33.61	11.14	5.19
4	0.007	0.008	0.010	0.017	1339.639	22.430	15.50	4.99	2.34
5	0.001	0.001	0.004	0.002	6229.091	10.895	7.50	1.13	NA‡
6	0.090	0.142	0.132	0.096	1442.000	138.400	146.33	47.42	21.64
7	0.004	0.008	0.019	0.022	1695.798	36.728	22.05	7.87	3.68
8	0.026	0.040	0.064	0.079	1498.959	118.818	90.56	31.19	14.21
9a†	0.003	0.006	0.021	0.014	2146.270	29.760	15.45	1.99	0.96
9b†	0.000	0.001	0.004	0.004	3680.858	16.379	7.21	5.16	2.43
10	0.213	0.318	0.323	0.201	1564.604	315.200	311.88	108.89	49.76
11	0.026	0.046	0.096	0.090	1759.473	157.967	125.04	38.01	17.66
12	0.004	0.006	0.009	0.012	2029.228	24.111	16.68	3.44	1.65
13	0.132	0.181	0.171	0.153	1324.263	202.912	NA	NA	NA
14	0.128	0.245	0.165	0.131	1434.611	187.871	NA	NA	NA
15	0.048	0.069	0.082	0.059	1579.918	93.452	NA	NA	NA
16a†	0.024	0.036	0.049	0.028	1257.590	35.411	NA	NA	NA
16b†	0.006	0.009	0.015	0.010	1333.514	13.844	NA	NA	NA
17	0.010	0.015	0.032	0.021	1556.026	33.013	NA	NA	NA
18	0.025	0.035	0.049	0.038	1470.284	56.596	NA	NA	NA

Subtitles 4× and 8× correspond to 4 and 8× background noise for thresholding methods. NA, not available; BMC, bone mineral content (total mineral mass); BMD, bone mineral density; Ca, calcium; P, phosphorous.

*Volume rounded to 3 decimal places for presentation in table

†2 separate specimens for subjects 9 and 16

‡sample size too small for accurate phosphorus quantitation

Arterioscler Thromb Vasc Biol. Author manuscript; available in PMC 2007 August 30.